NANO LETTERS

LETTER

pubs.acs.org/NanoLett

Reversible Nanopore Formation in Ge Nanowires during Lithiation–Delithiation Cycling: An In Situ Transmission Electron Microscopy Study

Xiao Hua Liu,[†] Shan Huang,[‡] S. Tom Picraux,[§] Ju Li,[‖,⊥] Ting Zhu,[*,‡] and Jian Yu Huang[*,†]

[†]Center for Integrated Nanotechnologies, Sandia National Laboratories, Albuquerque, New Mexico 87185, United States
[‡]Woodruff School of Mechanical Engineering, Georgia Institute of Technology, Atlanta, Georgia 30332, United States
[§]Center for Integrated Nanotechnologies, Los Alamos National Laboratory, Los Alamos, New Mexico 87545, United States
[‖]Department of Materials Science and Engineering, University of Pennsylvania, Philadelphia, Pennsylvania 19104, United States
[⊥]Department of Nuclear Science and Engineering and Department of Materials Science and Engineering, Massachusetts Institute of Technology, Cambridge, Massachusetts 02139, United States

S *Supporting Information*

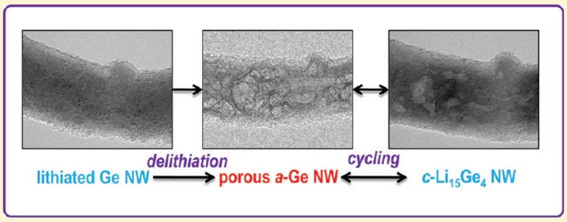

ABSTRACT: Retaining the high energy density of rechargeable lithium ion batteries depends critically on the cycle stability of microstructures in electrode materials. We report the reversible formation of nanoporosity in individual germanium nanowires during lithiation–delithiation cycling by in situ transmission electron microscopy. Upon lithium insertion, the initial crystalline Ge underwent a two-step phase transformation process: forming the intermediate amorphous Li$_x$Ge and final crystalline Li$_{15}$Ge$_4$ phases. Nanopores developed only during delithiation, involving the aggregation of vacancies produced by lithium extraction, similar to the formation of porous metals in dealloying. A delithiation front was observed to separate a dense nanowire segment of crystalline Li$_{15}$Ge$_4$ with a porous spongelike segment composed of interconnected ligaments of amorphous Ge. This front sweeps along the wire with a logarithmic time law. Intriguingly, the porous nanowires exhibited fast lithiation/delithiation rates and excellent mechanical robustness, attributed to the high rate of lithium diffusion and the porous network structure for facile stress relaxation, respectively. These results suggest that Ge, which can develop a reversible nanoporous network structure, is a promising anode material for lithium ion batteries with superior energy capacity, rate performance, and cycle stability.

KEYWORDS: Germanium nanowire, sponge, pore memory effect, reversible volume change, lithium ion battery, in situ TEM

Development of advanced lithium ion batteries (LIBs) requires new electrode materials with superior energy density, power density, and cycle stability. Germanium (Ge) is one of the most promising candidate anode materials with high volumetric capacity (7366 A h L^{-1}), second only to silicon (8334 A h L^{-1}).[1] Although the gravimetric capacity of Ge, 1384 mA h g^{-1},[2,3] is considerably lower than 3579 mA h g^{-1} of Si mainly due to the larger mass density, Ge has certain advantages as an anode material: (1) The capacity of Ge is significantly higher than the theoretical capacity of carbonaceous materials (372 mA h g^{-1}) used in current LIBs. (2) Ge has a higher intrinsic electronic conductivity due to its smaller band gap of 0.6 eV compared to Si.[4] (3) The diffusivity of Li in Ge is 400 times higher than in Si at room temperature,[5−7] allowing high rate capability demonstrated up to 1000C (1 C ≈ 1500 mA g^{-1}).[5] (4) Unlike Si, Ge does not form stable oxide on the surface and GeO$_x$ is water soluble.[4,5] Despite these merits, Ge has attracted much less attention than Si, probably due to its higher price, which may be reduced in the future because Ge is abundant in the Earth's crust.[5]

Herein, we report a detailed study of the lithiation/delithiation behavior of Ge nanowires (GeNWs) using in situ transmission electron microscopy (TEM).[8−15] For the first time, nanopore formation and spongelike segment growth during delithiation were directly recorded in real time. Fast reversible expansion and contraction of the nanowire during cycling, a "breathing" mode of electrochemically driven cyclic deformation, were also observed, indicating mechanical robustness and fast kinetics of a Ge anode in LIBs. Compared to the other materials (Si, Sn, SnO$_2$, ZnO, carbon nanotubes, etc.) studied with the same experimental setup,[8−15] GeNWs exhibit the highly desirable combination of high energy density, rate capability, and cycle stability and thus are promising anodes for advanced LIBs.

The GeNWs were synthesized using a chemical vapor deposition (CVD) method via the vapor–liquid–solid (VLS) mechanism. In a typical synthesis process, gold (Au, 100 nm in diameter) colloids were used as catalysts, over which a mixed gas of 300 sccm germane (GeH$_4$, 30% diluted in hydrogen, H$_2$) and 50 sccm phosphine (PH$_3$, 100 ppm in H$_2$) were flowing while the pressure was kept at 3 Torr. The temperature was first kept at

Received: July 14, 2011
Revised: August 16, 2011
Published: August 22, 2011

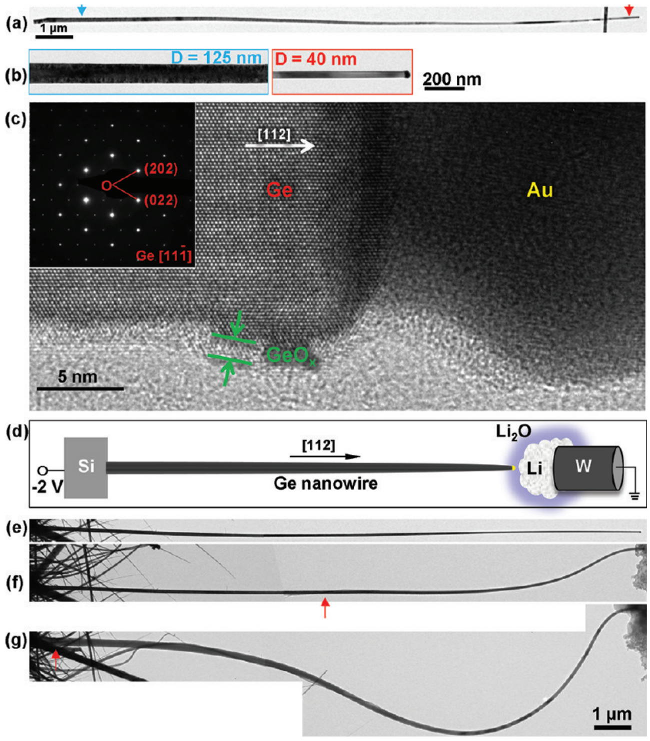

Figure 1. Morphology of Ge nanowires (GeNWs) before and after lithiation. (a−c) Typical microstructure of a pristine GeNW. (a) Low-magnification TEM image of a tapered GeNW. (b) Magnified images showing the thick root and thin tip of the GeNW, with diameters of 125 and 40 nm, respectively. (c) High-resolution image showing the GeNW grown along the [112] direction and with a 2 nm thick GeO$_x$ layer on the surface. The inset electron diffraction pattern (EDP) indicates that the GeNW is single crystalline. (d) Schematic illustration of the experimental setup for in situ electrochemical test. An individual GeNW is the working electrode, Li metal is the reference electrode, and the Li$_2$O layer on the Li metal is a solid electrolyte. (e-g) Typical morphology change during lithiation with both radial swelling and axial elongation. The pristine GeNW was straight (e) and bending deformation occurred during lithiation (f, g). The red arrows indicate the lithiation fronts.

365 °C for 90 s for nucleation, followed by growth at 275 °C for 70 min. All the in situ electrochemical tests were conducted in a Tecnai F-30 TEM operated at 300 kV with a Nanofactory TEM-scanning tunneling microscopy (STM) holder. Figure 1 shows a typical as-grown GeNW with a tapering morphology. The GeNWs were about 10 μm long (Figure 1a), with significantly different diameters from the root to the tip, being about 125 and 40 nm, respectively (Figure 1b), due to vapor−solid (VS) radial growth during the VLS growth process. The electron diffraction pattern (EDP) and high-resolution TEM image show that the GeNW was single-crystalline with a 2-nm thick GeO$_x$ layer on the surface (Figure 1c). The growth direction of the GeNWs was ⟨112⟩ of the diamond structure (Figure 1c). Figure 1d shows a schematic illustration of the experimental setup of an all solid nanobattery cell.[8,9,15] A piece of fresh Li metal was used as the reference electrode and lithium source, while a Li$_2$O layer served as the solid-state electrolyte to allow Li$^+$ transport.[8,9,15] This Li$_2$O layer was naturally grown on the surface of the Li metal during the sample transfer process from the glovebox to the TEM. During lithiation, a bias of −2 V was applied to the GeNWs with respect to the Li metal. Panels e−g of Figure 1 show the lithiation-induced morphology change of another GeNW, in which the red arrow marks the lithiation front. The pristine GeNW was straight (Figure 1e). During lithiation, the nanowire became thicker and bent as lithium was inserted into it (Figure 1f). After lithiation, the nanowire was significantly thickened and elongated (Figure 1g). In contrast to the little axial elongation in ⟨112⟩ SiNWs,[9,10] GeNWs always showed obvious elongation during lithiation.

Figure 2 shows a close view of the microstructure evolution of the Ge NWs during lithiation. The single crystalline Ge (*c*-Ge) nanowire was gradually converted to an amorphous Li$_x$Ge (*a*-Li$_x$Ge) nanowire in a core−shell mode when the lithiation front moved radially from the nanowire surface toward the center (Figure 2a−d). Meanwhile, the diameter increased from 39 to 67 nm at the marked location. This stage of phase transformation involved the electrochemically driven solid state amorphization (ESA), as similarly occurring to the SiNWs.[9,10] Subsequently, the *a*-Li$_x$Ge alloy quickly crystallized to a single crystalline nanowire, and the nanowire diameter further expanded to 83 nm at the same marked place (Figure 2e). The above sequential phase transformations of c-Ge $\rightarrow$ a-Li$_x$Ge $\rightarrow$ c-Li$_{15}$Ge$_4$ were identified by the EDPs (Figure 2f−h), consistent with the in situ X-ray diffraction results from conventional electrochemical tests.[2,3,5] Figure 2i shows a magnified TEM image of another GeNW during the ESA process, which clearly resolves the core−shell structure: *c*-Ge in the center, wrapped by thick *a*-Li$_x$Ge, Li$_2$O on the surface with a thickness of ∼5 nm. The Li$_2$O layer was crystalline, as shown in the EDPs (Figure 2g,h). The lithiation process of GeNWs shows similar features as the SiNWs in terms of the phase transformation sequence and the core−shell structure.[9,10] Like Si, Ge also undergoes a two-step lithiation process: M $\rightarrow$ a-Li$_x$M $\rightarrow$ c-Li$_{15}$M$_4$ (M = Si or Ge). The intermediate amorphous Li$_x$M phase has a large solubility range (Δx) for lithium and at higher x can be structurally and chemically similar to the final crystallized Li$_{15}$M$_4$ phases.[9,10,16−20] The similar development of the core−shell structure indicates a considerably higher rate of surface transport of Li$^+$ ions than bulk transport in the first lithiation process. However, there are obvious differences in the morphological changes between lithiated Si and Ge, as discussed next.

Figure 3 shows the delithiation process of the lithiated GeNWs. During the delithiation, a bias of +2 V was applied on the Li$_{15}$Ge$_4$ NWs with respect to the Li metal. When the lithium extraction begun, volume shrinkage was instantly seen near the contact between the nanowire and Li$_2$O (Figure 3a,b and Movie S2, see Supporting Information). Shortly after that, nanopores emerged in the shrunken region, and such a nanoporous region propagated toward the other end at a speed of ∼5 nm/s (Figure 3c−f), forming a moving "delithiation front", which was a visible interface between a remarkable porous region and the dense Li$_{15}$Ge$_4$ nanowire. Figure 3g−j and Movie S3 (Supporting Information) show the similar rapid propagation of a delithiation front along another nanowire. The formation of the porous structure and delithiation front can be attributed to the fast rate of the long-range transport of Li$^+$, as well as the fast local aggregation of lithium extraction-produced vacancies to form pores, to be further studied by our theoretical modeling. Since pores nucleated and grew quickly, the nanowire did not shrink to a solid thinner wire but formed a spongelike network with many pores.

It is important to note that the delithiated porous nanowire did not fracture. Moreover, repeated cycles of lithium insertion and extraction, accompanied with reversible volume changes resembling

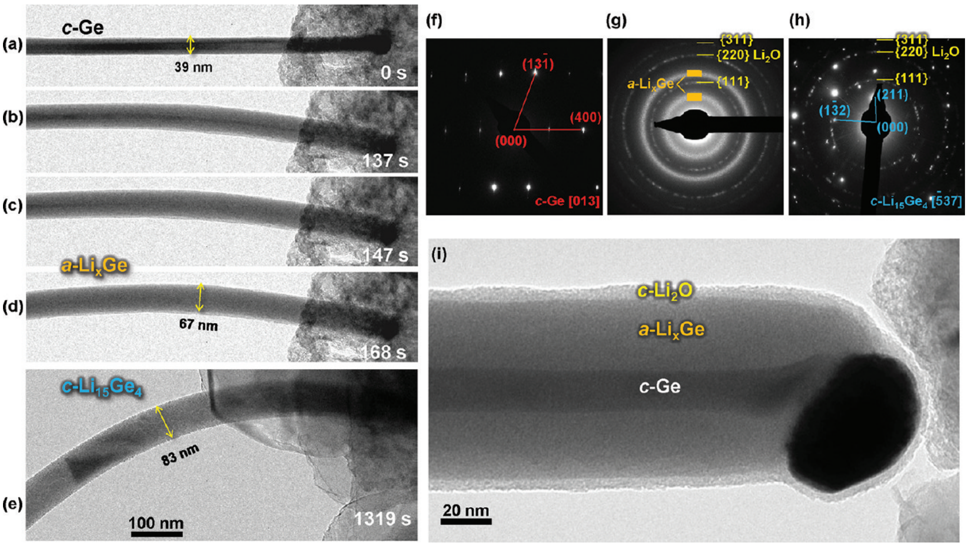

Figure 2. Microstructure evolution during lithiation of the GeNW. (a−e) Morphological evolution of a segment of the GeNW. The pristine single crystalline Ge (*c*-Ge) nanowire was straight with a diameter of 39 nm at the marked cross section (a). Lithiation begun from the nanowire surface and the reaction front propagates toward the center (b−d), resulting in a gray contrast due to the formation of amorphous Li$_x$Ge (*a*-Li$_x$Ge). The diameter increased to 67 nm (d). Finally the nanowire showed a crystalline contrast again and the diameter further increased to 83 nm (e). (f−h) EDPs showing the sequential phase transformations from *c*-Ge (f) via *a*-Li$_x$Ge (g) to the fully lithiated single crystalline Li$_{15}$Ge$_4$ (*c*-Li$_{15}$Ge$_4$) phases (h). The diffraction rings in (g) and (h) were from Li$_2$O. (i) High-magnification image showing the intermediate state during lithiation. From the center to the surface, the layers were a *c*-Ge core, an *a*-Li$_x$Ge shell, and a *c*-Li$_2$O layer (∼5 nm thick).

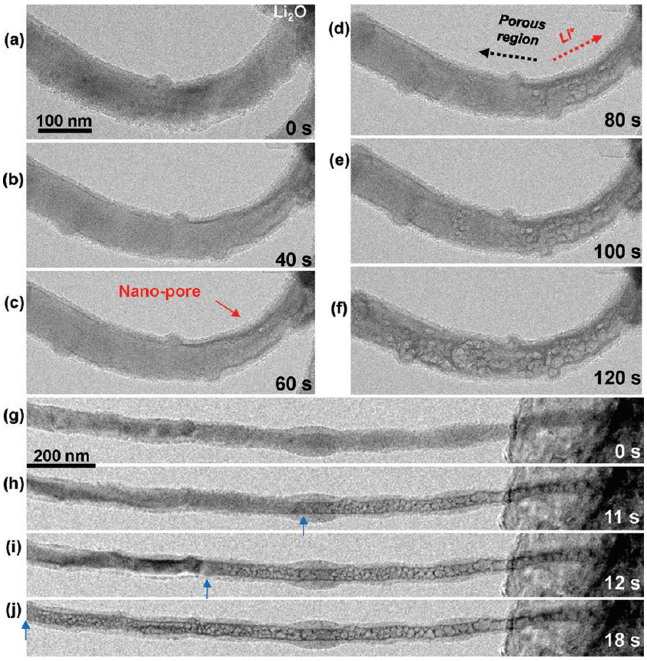

Figure 3. Nanopore formation and evolution during delithiation. (a−f) Nucleation of nanopores during the initial stage of delithiation: (a) a lithiated nanowire; (b) the end of the nanowire contacting Li$_2$O/Li started to shrink due to the Li$^+$ extraction; (c) nanopore emerged in the shrunk region as Li$^+$ ions were further extracted; (d−f) propagation of the nanoporous region. (g−j) Extension of the nanoporous region during delithiation of another nanowire. The blue arrows indicate the "delithiation fronts", i.e., the boundaries between the nanoporous regions and the Li$_{15}$Ge$_4$ segments (h−j).

the "breathing" behavior, were observed (Figure 4a−h and Movie S4, see Supporting Information). For the segment in the field of view with a length of ∼1 μm, each cycle completed within 1 min, and reversible phase transformation between the *c*-Li$_{15}$Ge$_4$ and *a*-Ge phases was achieved (Figure 4i−n). This in situ multicycling test shows an amazingly robust and reversible process of cyclic lithium insertion and extraction in the GeNWs. Although the conventional electrochemical characterizations of single GeNWs based on the current/voltage profiles were not available yet, structural analyses unambiguously indicated the completely reversible conversions between Li$_{15}$Ge$_4$ and Ge, consistent with the high electrochemical performance of bulk GeNWs grown by the similar CVD method.[6]

The electrochemical behavior of the GeNWs showed different characteristics from Si: First, the lithiation-induced swelling in the cross section of crystalline GeNWs was much less anisotropic than SiNWs. This suggests that the mobility of the sweeping lithiation front (i.e., the two-phase interface between the crystalline core and amorphous shell) is less sensitive to the interface orientation, considering that the large lithiation strain is expected to occur primarily at the sharp two-phase interface and tend to align locally with the interfacial normal.[9,21] These trends are consistent with the much less anisotropy of the interfacial reaction rate in Ge than Si in the wet-etching experiments.[22,23] Second, an axial delithiation front, characterized by the formation of nanopores in its wake, was clearly visible in Ge since the first delithiation cycle. In Si, nanopores were not observed in the first few delithiation cycles. Nanoporous formation in crystalline Ge (but not Si) was also observed during room temperature ion implantation at high fluences after Ge amorphizes due to vacancy agglomeration.[24,25] Third, single crystalline Li$_{15}$Ge$_4$ nanowire (Figures 2h and 4n) formed in Ge after lithiation, in contrast to the polycrystalline Li$_{15}$Si$_4$ or amorphous Li$_x$Si nanowire formed after lithiation of Si nanowires,[9,10] probably due to the much higher diffusivity of Li in Ge (and Li$_x$Ge) that facilitates the atomic rearrangement during crystallization. The intrinsically excellent electrical conductivity of Ge, fast cycling kinetics, and reversible porous structures indicate that Ge is an excellent anode

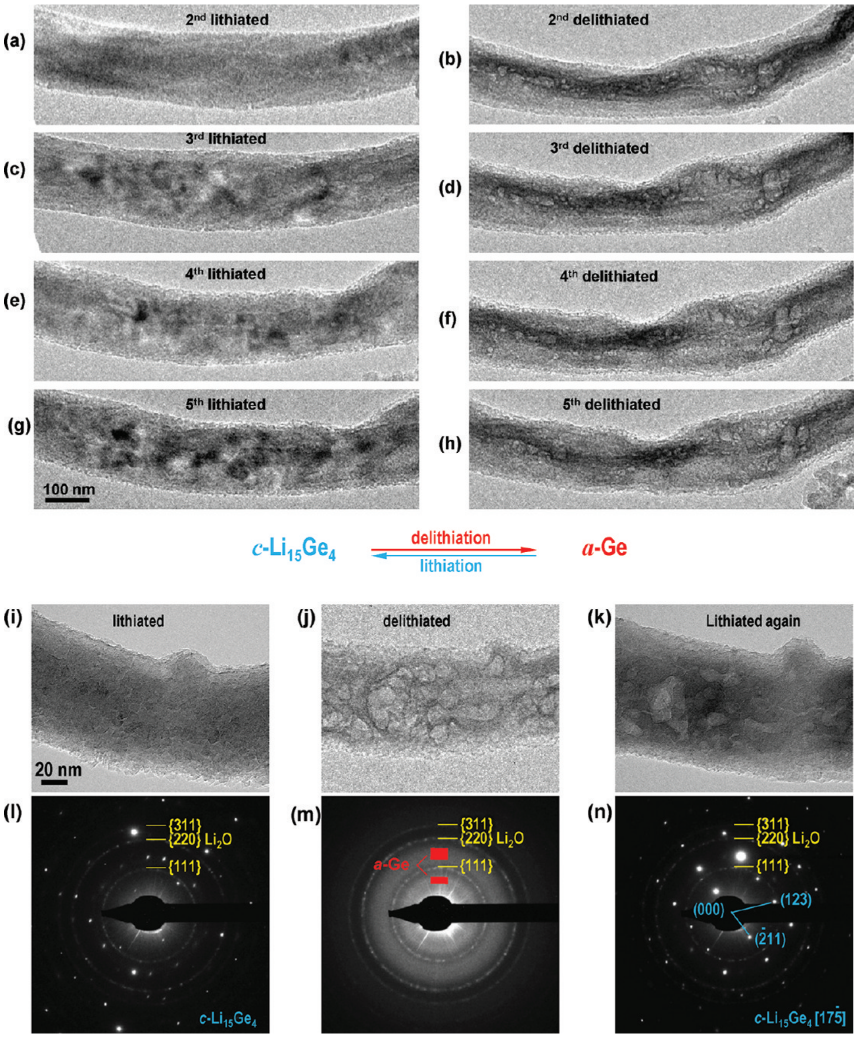

Figure 4. Microstructure evolution of a GeNW during cycling. (a–h) Reversible volumetric changes in four sequential lithiation/delithiation cycles. After each lithiation process, the nanowire was thickened and showed a crystalline contrast (a, c, e, g). After each delithiation process, the nanowire shrunk, became porous, and exhibited an amorphous contrast (b, d, f, h). The position and distribution of the nanopores were almost unchanged. (i–n) Close view at the microstructure changes in the lithiation/delithiation cycles. (i–k) High magnification images showing the morphology changes at the same place of a nanowire. (l–n) EDPs showing reversible phase transformation between the c-$Li_{15}Ge_4$ (lithiated) and a-Ge (delithiated) phases during cycling.

candidate with high energy density, power density, and cycle stability for lithium ion batteries, as shown in the electrochemical measurements of Ge electrode-based batteries in earlier work.[2,3,5,6,26−30]

Another striking phenomenon seen in the TEM is the so-called "pore memory effect" (PME) during cycling. The lithiated c-$Li_{15}Ge_4$ NWs (Figure 4c,e,g) are rather dense with single-crystal orientation. When they were delithiated, many pores of nearly the same sizes and shapes (compare panels d, f, and h of Figure 4) reappeared at the same old locations. This means "memories" of previous pores must be somehow retained in the crystalline configurations (Figure 4c,e,g), despite multiple crystallization−amorphization cycles and large conformation changes (reversible local strain on the order of 100%). A likely explanation for PME is that (a) after the pores were first created, Li diffusion occurred preferentially along free surface of internal pores (surface diffusion is much faster than bulk diffusion), thus regions near the pore were first lithiated and delithiated in subsequent cycles, like the alveoli of a lung, and (b) during lithiation, the pores were greatly constricted, but never fully closed, so when delithiation started, the pores could recover their old tracks. Besides scientific interest, PME should be important for modeling electrode damage. PME also means that the first few cycles of an electrode (break-in period) are critically important for the subsequent behavior of the electrode, since they establish a long-memory microstructural pattern that persists.

To understand the pore formation mechanism in the first cycle, a continuum phase field model was developed to simulate the delithiation-induced microstructure evolution. During delithiation, nanopores form because the electrochemical extraction of Li produces vacancies that aggregate into clusters, similar to the formation of porous metals in dealloying.[31] This porosity formation process is an intrinsically multiscale phenomenon, involving the local selective dealloying of Li, aggregation of vacancies, and long-range transport of Li. Our phase field modeling focused on the first two local processes in a representative volume element (RVE), which was considered as an open system undergoing the porosity formation driven by Li extraction

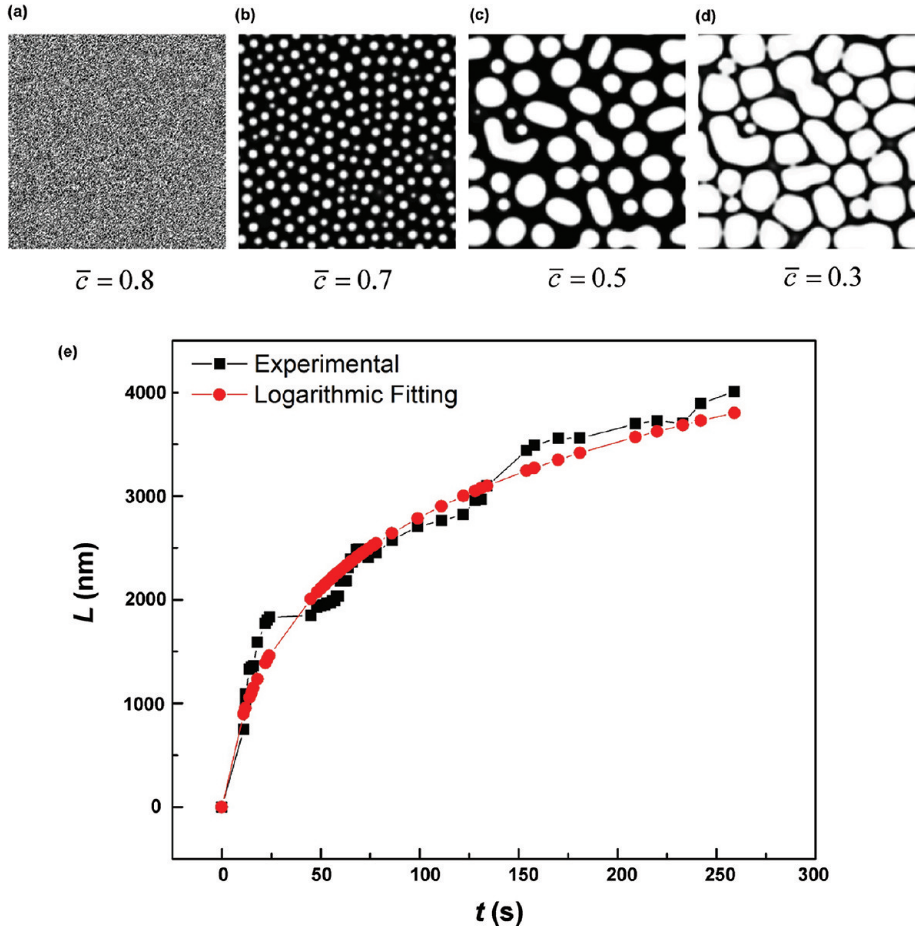

$\bar{c} = 0.8$ $\bar{c} = 0.7$ $\bar{c} = 0.5$ $\bar{c} = 0.3$

Figure 5. Modeling of porosity formation and the time law of propagation of the nanoporous region during delithiation. (a–d) Phase field simulation showing the nucleation and growth of nanopores in a representative volume element (RVE) during Li extraction. The grayscale indicates the local concentration of the Li–Ge alloy $c(x,y,t)$, i.e., fraction of the atomic sites occupied by the Li–Ge alloy; $c \approx 1$ (black) represents the Li–Ge alloy phase at the fully lithiated state and $c \approx 0$ (white) the pore. $\bar{c}(t)$ is the average fraction of atomic sites occupied by the Li–Ge alloy in the RVE, and it decreases due to Li extraction from the RVE. Correspondingly, the ratio of Li to Ge in the Li–Ge alloy phase changes with $\bar{c}(t)$. For example, when $\bar{c}(t) = 1$, the Li–Ge alloy is $Li_{3.75}Ge$, and when $\bar{c}(t) = 0.21$, it is pure Ge. (e) $L-t$ curve (L, length of the porous region; t, time), showing the time law of the delithiation front sweeping along the nanowire. Some of the corresponding TEM images are shown in Figure 3g–j. The red line is plotted on the basis of logarithmic fitting, in agreement with the experimental results (black squares).

(Supporting Information). Specifically, we note that the development of a core–shell structure during lithiation suggested the greater diffusivity of Li on the surface than in the bulk. Thus it is plausible to suppose the Li atoms leave a local volume through a fast diffusion path along the surface of percolated pores. The subsequent local rearrangement of atoms causes aggregation of vacancies and thus growth of pores. A further increase of pore sizes occurs by coalescence of small pores, for reducing the total surface area and thus lowering the surface energy in the system. This was simulated as a dynamic phase separation process based on a free energy function with double wells, giving a segregated mixture of two phases:[32] one is the vacancy (forming pores) and the other is the homogeneous Li–Ge alloy (forming interconnected ligaments). To mimic Li extraction, the average fraction of atomic sites occupied by the Li–Ge alloy in the RVE, denoted as $\bar{c}(t)$, was assumed to decease with time, and correspondingly that by vacancies, $1 - \bar{c}(t)$, increased oppositely because of the conservation of atomic sites—this site conservation assumption is a first-order approximation to capture the dominant delithiation response of porosity formation by neglecting the loss of atomic sites due to less significant volume reduction as observed in experiments.

Figure 5 shows the phase field simulation results of nucleation and growth of nanopores during Li extraction. The simulated pore morphology is qualitatively consistent with that observed through in situ TEM experiments. The characteristic length scale of nanoporosity, i.e., mean pore size, is controlled by the dynamic interplay between the rate of Li extraction in the RVE and the rate of pore growth, i.e., phase coarsening. As discussed earlier, the former rate is presumably governed by Li transport through a percolating path along the pore surface, and the latter is dictated by both the effective atomic mobility in the Li–Ge alloy and the surface energy of nanopores. Numerical studies indicate that atomic mobilities must decrease drastically with decreasing Li fraction. In other words, in the late stage of delithiation, it is necessary to kinetically freeze the porous structure for retaining a well-connected network of Ge ligaments between large pores. This slowdown of diffusional flow with decreasing Li concentration can be physically interpreted as transition from the Li-mediated to Ge-dominated diffusion. The latter is expected to be slow when the assistance of "lubricating" Li on diffusion is lacking.[33] It has been discussed earlier that the nanoporous structure provides a mechanically robust network to accommodate large strains during repeated lithiation. These modeling results imply that the nanoporosity control may be achieved through tuning the atomic mobilities by means of, for example, doping.[10]

In addition to gaining insights into nanoporosity formation, our theoretical analysis of the long-range transport of Li also provides a physical rationale for the measured logarithmic time law of motion of the delithiation front (i.e., a sharp interface separating the dense and porous segments in the wire). Figure 5e shows the measured $L-t$ data (L being length of the nanoporous segment and t being time) of the nanowire whose TEM images have been shown in Figure 3g–j. These data can be well fitted by a logarithmic relationship of $L = A\ \ln(Bt + 1)$, with the fitting constants $A = 1117$ nm and $B = 0.1122$/s. As discussed earlier, Li atoms are expected to leave a local volume along a fast diffusion path on the surface of a percolating pore. For a short porous segment, L, all the pores can connect through from Li source to drain. As L gets longer, we lose more percolating paths, and the number of fast diffusion paths directly connecting source to drain is expected to fall off as $N \propto e^{-L/A}$, where A is the characteristic end-to-end length of a multiple-connected pore. Thus in this initial regime of delithiation, $\mathrm{d}L/\mathrm{d}t \propto N \propto e^{-L/A}$, and integration of the foregoing relation gives the logarithmic rate equation of the form $L = A\ \ln(Bt + 1)$. This is similar to an argument of the blockage of the "leakage spots" previously used for modeling oxidation.[34,35] Compared to the commonly used parabolic time law,[36] the logarithmic relation enables an improved fitting of experimental data, thereby providing a more physically reasonable correlation between the time law of delithiation dynamics with the state-and-rate effect of morphological evolution on the long-range Li transport.

Our findings provide new insights into the mechano-electrochemical behavior in the Ge electrodes. Resembling a reversible sponge, the porous *a*-Ge nanowire was a three-dimensional (3D) interconnected network, which showed similar morphology (pore size and distribution) after each delithiation process (panels b, d, f, and h in Figure 4). Importantly, unlike Si, cracks were never observed in the lithiation/delithiation cycles of Ge nanowires. This indicated that the internal amorphous Ge network was stable and robust. Instead of dramatic, overall geometric changes, the volume changes during cycling were accommodated by porosity changes, i.e., higher porosity when delithiated. As a result, the nominal diameter change was not large after the first cycle when the network was formed (Figure 4). Furthermore, the formation of pores in Ge occurs via aggregation of the delithiation generated vacancies. It is an effective mechanism of stress relaxation, requiring the relatively fast short-range diffusion of vacancies and/or host atoms (Ge) compared to the large-range transport of Li to its drain. In contrast, the often observed cracking in Si during delithiation would require the buildup of high tensile stresses due to the ineffective stress relaxation (e.g., local trapping of delithiation-generated vacancies).[37] The mechanical robustness of porous Ge can be understood in the following three aspects: (1) The tiny Ge ligaments of the 3D network were nanowires with smaller diameters (on the order of several to 10 nm) than that of the original nanowire and thus are more favorable for facile stress release. (2) Within the network of the sponge, material addition and removal occur locally without large deformation of the ligaments. (3) High electronic conductivity and Li diffusivity in Ge allow fast kinetics and avoid composition heterogeneity that could induce internal stress. Therefore, once the network was formed, it enabled reversible and fast lithiation/delithiation of the spongelike nanostructure. In a real lithium ion battery, such property could be highly beneficial, because the nanoporous sponge provides continuous electrical conduction and ion transport paths, thus facilitating fast ion transport, facile stress release, and cycle stability of microstructures. Because the sponge contained plenty of voids, the nominal volume change during lithiation is not significant, minimizing the mechanical degradation during cycling. In practice, a Ge anode with preloaded Li can be used for fabrication of the battery,[38] as the porous Ge produced by prelithiation may exhibit high mechanical stability, energy density, and rate performance.

Conclusions. In summary, the electrochemical lithiation/delithiation behavior of individual Ge nanowires was studied with in situ transmission electron microscopy. The results confirmed the $Li_{15}Ge_4$ phase as the final lithiated product and were consistent with recent electrochemical tests on conventional Ge electrodes. After delithiation, the Ge nanowires were converted to a nanoporous sponge composed of interconnected ligaments of amorphous Ge. For the first time, nanopore formation and propagation were observed in real time during delithiation, providing important insight into the mechanism of microstructural evolution in Ge electrodes. Fast cycling was demonstrated for the Ge nanowires with reversible porous structures. These results indicate that Ge is an excellent anode candidate with high energy density, power density, and mechanical robustness for advanced lithium ion batteries.

■ ASSOCIATED CONTENT

Ⓢ Supporting Information. The phase field simulation details and three movies showing the nanopore nucleation, propagation, and multicycling of GeNWs, respectively. This material is available free of charge via the Internet at http://pubs.acs.org.

■ AUTHOR INFORMATION

Corresponding Authors

*E-mail: jhuang@sandia.gov; ting.zhu@me.gatech.edu.

■ ACKNOWLEDGMENT

Portions of this work were supported by a Laboratory Directed Research and Development (LDRD) project at Sandia National Laboratories (SNL) and partly by Nanostructures for Electrical Energy Storage (NEES), an Energy Frontier Research Center (EFRC) funded by the U.S. Department of Energy, Office of Science, Office of Basic Energy Sciences under Award Number DESC0001160. The LDRD supported the development and fabrication of platforms. The NEES center supported the development of TEM techniques. CINT supported the TEM capability, in addition, this work represents the efforts of several CINT users, primarily those with affiliation external to Sandia National Laboratories. In addition, this work was performed, in part, at the Sandia—Los Alamos Center for Integrated Nanotechnologies (CINT), a U.S. Department of Energy, Office of Basic Energy Sciences user facility. Sandia National Laboratories is a multiprogram laboratory managed and operated by Sandia Corporation, a wholly owned subsidiary of Lockheed Martin

Company, for the U.S. Department of Energy's National Nuclear Security Administration under Contract DE-AC04-94AL85000. T.Z. acknowledges the support by NSF Grants CMMI-0758554 and 1100205. J.L. acknowledges support by NSF DMR-1008104 and AFOSR FA9550-08-1-0325.

REFERENCES

(1) Larcher, D.; Beattie, S.; Morcrette, M.; Edstroem, K.; Jumas, J. C.; Tarascon, J. M. *J. Mater. Chem.* **2007**, *17* (36), 3759–3772.

(2) Baggetto, L.; Notten, P. H. L. *J. Electrochem. Soc.* **2009**, *156* (3), A169–A175.

(3) Baggetto, L.; Hensen, E. J. M.; Notten, P. H. L. *Electrochim. Acta* **2010**, *55* (23), 7074–7079.

(4) Wang, D. W.; Chang, Y. L.; Wang, Q.; Cao, J.; Farmer, D. B.; Gordon, R. G.; Dai, H. J. *J. Am. Chem. Soc.* **2004**, *126* (37), 11602–11611.

(5) Graetz, J.; Ahn, C. C.; Yazami, R.; Fultz, B. *J. Electrochem. Soc.* **2004**, *151* (5), A698–A702.

(6) Chan, C. K.; Zhang, X. F.; Cui, Y. *Nano Lett.* **2008**, *8* (1), 307–309.

(7) Fuller, C. S.; Severiens, J. C. *Phys. Rev.* **1954**, *96* (1), 21–24.

(8) Liu, X. H.; Huang, J. Y. *Energy Environ. Sci.* **2011**, DOI: 10.1039/C1EE01918J.

(9) Liu, X. H.; Zheng, H.; Zhong, L.; Huang, S.; Karki, K.; Zhang, L. Q.; Liu, Y.; Kushima, A.; Liang, W. T.; Wang, J. W.; Cho, J.-H.; Epstein, E.; Dayeh, S. A.; Picraux, S. T.; Zhu, T.; Li, J.; Sullivan, J. P.; Cumings, J.; Wang, C.; Mao, S. X.; Ye, Z. Z.; Zhang, S.; Huang, J. Y. *Nano Lett.* **2011**, *11* (8), 3312–3318.

(10) Liu, X. H.; Zhang, L. Q.; Zhong, L.; Liu, Y.; Zheng, H.; Wang, J. W.; Cho, J.-H.; Dayeh, S. A.; Picraux, S. T.; Sullivan, J. P.; Mao, S. X.; Ye, Z. Z.; Huang, J. Y. *Nano Lett.* **2011**, *11* (6), 2251–2258.

(11) Huang, J. Y.; Zhong, L.; Wang, C. M.; Sullivan, J. P.; Xu, W.; Zhang, L. Q.; Mao, S. X.; Hudak, N. S.; Liu, X. H.; Subramanian, A.; Fan, H. Y.; Qi, L.; Kushima, A.; Li, J. *Science* **2010**, *330* (6010), 1515–1520.

(12) Zhong, L.; Liu, X. H.; Wang, G. F.; Mao, S. X.; Huang, J. Y. *Phys. Rev. Lett.* **2011**, *106* (24), 248302.

(13) Zhang, L. Q.; Liu, X. H.; Liu, Y.; Huang, S.; Zhu, T.; Gui, L.; Mao, S. X.; Ye, Z. Z.; Wang, C. M.; Sullivan, J. P.; Huang, J. Y. *ACS Nano* **2011**, *5* (6), 4800–4809.

(14) Liu, X. H.; Zhong, L.; Zhang, L. Q.; Kushima, A.; Mao, S. X.; Li, J.; Ye, Z. Z.; Sullivan, J. P.; Huang, J. Y. *Appl. Phys. Lett.* **2011**, *98* (18), 183107.

(15) Liu, Y.; Zheng, H.; Liu, X. H.; Huang, S.; Zhu, T.; Wang, J.; Kushima, A.; Hudak, N. S.; Huang, X.; Zhang, S.; Mao, S. X.; Qian, X.; Li, J.; Huang, J. Y. *ACS Nano* **2011**, DOI: 10.1021/nn202071y.

(16) Gladyshevskii, E. I.; Kripyakevich, P. I. *Sov. Phys., Crystallogr.* **1960**, *5* (4), 549–551.

(17) Johnson, Q.; Smith, G. S.; Wood, D. *Acta Crystallogr.* **1965**, *18*, 131–132.

(18) Hatchard, T. D.; Dahn, J. R. *J. Electrochem. Soc.* **2004**, *151* (6), A838–A842.

(19) Obrovac, M. N.; Christensen, L. *Electrochem. Solid-State Lett.* **2004**, *7* (5), A93–A96.

(20) Obrovac, M. N.; Krause, L. J. *J. Electrochem. Soc.* **2007**, *154* (2), A103–A108.

(21) Hsueh, C. H.; Evans, A. G. *J. Appl. Phys.* **1983**, *54* (11), 6672–6686.

(22) Leancu, R.; Moldovan, N.; Csepregi, L.; Lang, W. *Sens. Actuators, A* **1995**, *46* (1−3), 35–37.

(23) Schwartz, B. *J. Electrochem. Soc.* **1967**, *114* (3), 285–292.

(24) Stritzker, B.; Elliman, R. G.; Zou, J. *Nucl. Instrum. Methods Phys. Res., Sect. B* **2001**, *175*, 193–196.

(25) Ottaviano, L.; Verna, A.; Grossi, V.; Parisse, P.; Piperno, S.; Passacantando, M.; Impellizzeri, G.; Priolo, F. *Surf. Sci.* **2007**, *601* (13), 2623–2627.

(26) Chae, O. B.; Park, S.; Ku, J. H.; Ryu, J. H.; Oh, S. M. *Electrochim. Acta* **2010**, *55* (8), 2894–2900.

(27) Hwa, Y.; Park, C. M.; Yoon, S.; Sohn, H. J. *Electrochim. Acta* **2010**, *55* (9), 3324–3329.

(28) Kim, Y.; Hwang, H.; Lawler, K.; Martin, S. W.; Cho, J. *Electrochim. Acta* **2008**, *53* (15), 5058–5064.

(29) Park, M. H.; Kim, K.; Kim, J.; Cho, J. *Adv. Mater.* **2010**, *22* (3), 415–418.

(30) Seo, M. H.; Park, M.; Lee, K. T.; Kim, K.; Kim, J.; Cho, J. *Energy Environ. Sci.* **2011**, *4* (2), 425–428.

(31) Erlebacher, J.; Aziz, M. J.; Karma, A.; Dimitrov, N.; Sieradzki, K. *Nature* **2001**, *410* (6827), 450–453.

(32) Lu, W.; Suo, Z. *J. Mech. Phys. Solids* **2001**, *49* (9), 1937–1950.

(33) Huang, S.; Zhu, T. *J. Power Sources* **2011**, *196* (7), 3664–3668.

(34) Davies, D. E.; Evans, U. R.; Agar, J. N. *Proc. R. Soc. A* **1954**, *225* (1163), 443–462.

(35) Lawless, K. R. *Rep. Prog. Phys.* **1974**, *37* (2), 231–316.

(36) Deal, B. E.; Grove, A. S. *J. Appl. Phys.* **1965**, *36* (12), 3770–3778.

(37) Chon, M. J.; Sethuraman, V. A.; McCormick, A.; Srinivasan, V.; Guduru, P. R. *Phys. Rev. Lett.* **2011**, *107* (4), 045503.

(38) Liu, N.; Hu, L.; McDowell, M. T.; Jackson, A.; Cui, Y. *ACS Nano* **2011**, *5* (8), 6487–6493.